

Modeling of SPS Apparatus: Temperature, Current and Strain Distribution with No Powders

A. Cincotti, A. M. Locci, R. Orrù, and G. Cao

Dipartimento di Ingegneria Chimica e Materiali, Centro Studi sulle Reazioni Autopropaganti (CESRA), Centro LINCE del Consorzio Interuniversitario Nazionale di Scienza e Tecnologia dei Materiali (INSTM), Università degli Studi di Cagliari, Piazza d'Armi, 09123 Cagliari, Italy

DOI 10.1002/aic.11102

Published online January 22, 2007 in Wiley InterScience (www.interscience.wiley.com).

The mathematical simulation of the spark plasma sintering/synthesis (SPS) apparatus, which represents an effective tool for sintering/synthesizing advanced materials, is addressed. Because several, concomitant physicochemical phenomena—such as heat transfer and generation, electric current transport, and stress–strain mechanics along with chemical transformation and sintering—take place during SPS processes, a step-by-step heuristic procedure is proposed for successful quantitative modeling purposes. First, in this work we consider the SPS behavior of specific sample configurations characterized by the absence of powders. This approach permits detailed analysis of the system from the perspective of electric phenomena. The inductive character is carefully described and properly taken into account when comparing experimental data with model results. The importance of considering rms (root mean squared) electric current for a quantitative determination of the Joule effect is highlighted. Moreover, this approach allows one to determine the electric and thermal resistances experimentally evidenced in the horizontal contacts between stainless steel electrodes and graphite spacers as functions of temperature and applied mechanical load. Horizontal contact resistances between graphite elements are experimentally found to be negligible and, accordingly, they are not modeled. Model reliability is tested by comparing numerical simulations with experimental data obtained at operating conditions far from those adopted during the fitting procedure of unknown parameters. The proposed model can be successfully compared from a quantitative perspective to the measured temperature, voltage, and displacement, once rms current, geometry, and mechanical load are set. © 2007 American Institute of Chemical Engineers AIChE J, 53: 703–719, 2007

Keywords: spark plasma sintering, modeling, heat transfer, Joule heating, electric current transport, stress–strain mechanics

Introduction

Spark plasma sintering/synthesis (SPS), an effective process for the sintering/synthesis of advanced materials such as ceramics, metals, polymers, and semiconductors,^{1–3} basically consists in heating up the powder sample shaped into a die inserted between two water-cooled electrodes (rams) by means

of a pulsed electric DC forced to pass through, while uniaxially pressing the system to facilitate sintering processes and guarantee electric circuit closure. A few thousands of amperes of average electric current and a few tens of volts of average voltage across the electrical load comprising the two rams, from 3 to a few hundred kilonewtons (kN) of applied mechanical load, are the typical operative conditions adopted in SPS processes. In the technical literature, SPS is considered a thermoefficient sintering process because highly dense products in relatively short times are attainable.^{1,2,4–8} A volumic heating rate resulting from the Joule effect—in contrast to the conductive heat transport applied in conventional sintering systems—

Correspondence concerning this article should be addressed to A. Cincotti at cincotti@visnu.dicm.unica.it or G. Cao at cao@visnu.dicm.unica.it
G. Cao is also affiliated with CRS4, Centro di Ricerca, Sviluppo e Studi Superiori in Sardegna, Parco Scientifico e Tecnologico, Polaris, Edificio 1, 09010 PULA (CA), Italy.

permits a rapid increase in temperature that is able to enhance the mass transport mechanisms responsible for sintering phenomena, thus improving the consolidation rate and minimizing grain coarsening. The latter aspect leads to improved mechanical, physical, and optical properties of final sintered products.¹

However, to explain surface effects found experimentally (that is, clean grain boundaries in final sintered specimens), an additional spark/plasma mechanism has been assumed,² thus justifying the use of an electric current flowing as a train of pulses through the powder sample. Briefly, even a few thousands of amperes and tens of volts could be able to provoke arcing between powder particles in point contact (seen as a network of capacitors facing each other), with the corresponding material transfer from cathode to anode. This should be responsible for the electric discharges (spark) and the subsequent high current density could generate a localized Joule effect, which in turn allows evaporation of the material particle (plasma), thus enhancing the transport mechanism and sintering rate. Although the preceding explanation is still controversial,^{1,5,6,8,9} the occurrence of clean grain boundaries in final sintered products was reported to be associated with the thermal and electric breakdown of oxide insulating films typically covering powder particles.

Moreover, apart from this electric perspective related to the “capacitive” character of a network of sintering powders, the intrinsic influence of electric field on crystal defect motion, crystal nucleation and growth, phase transformation, and plastic deformation could be reasonably taken into account when investigating SPS processes.^{7,10}

From this picture, it is clear that different physicochemical phenomena—that is, heat transport and generation, electric current transport, and stress–strain mechanics, along with sintering and synthesis—are involved and complexly coupled in SPS processes. Appropriate modeling strategies can thus be adopted for guiding scaling-up design procedures not only to identify optimized operative conditions (that is, relative sizes, mechanical load, power input) but also to attempt solving some unanswered questions related to the physicochemical phenomena actually taking place during SPS processes.

However, this general objective can be reached only when quantitative comparison between modeling results and experimental data will be possible. On the other hand, this goal is still missing in the relatively limited number of literature articles addressing modeling of the SPS system. Apart from models that admit analytical solutions that are able to provide only qualitative descriptions of system behavior,^{4,6} a few recent and more complex models are capable of simulating, once solved numerically, temperature and electric current distributions.^{8,9,11} In particular, Zavaliangos et al.¹¹ were the first who recognized the importance of contact resistances in SPS systems and tried to evaluate them. Horizontal and vertical contact resistances (both thermal and electric) were fitted together, without explicitly determining their temperature and/or mechanical load dependencies. Indeed, constant values of thermal and electric contact resistances are not adequate for quantitative modeling purposes, especially when considering different applied mechanical load levels. Moreover, no discrimination between graphite–graphite and graphite–stainless steel contact resistances was made. Actually, electrodes were modeled by considering them as made of monolithic graphite elements, without taking into account the heat removal by cooling water flowing inside tubes drilled into the rams.

The contribution of contact resistances was neglected by Anselmi-Tamburini et al.,⁹ whereas the differences in Joule heat generation and related temperature distribution were taken into account, when a monolithic electric conductor (copper) and resistor (alumina) were used as the SPS specimen inside a graphitic die. Actually, this aspect was already emphasized by Heian et al.¹² in their modeling of the synthesis of MoSi₂/SiC composites through SPS.

The presence of stainless steel electrodes was not accounted for by Vanmeensel et al.,⁸ who considered an anisotropic graphite foil sandwiched at every contact, in both the vertical and the horizontal positions. The related thermal and electric contact resistances were modeled through thin-film approximation. The parameters corresponding to horizontal and vertical contact resistances, respectively, were fitted against experimental data, by properly considering the SPS system with added contact interfaces. However, the corresponding dependency from the applied mechanical load was neglected, whereas the temperature contribution was determined by fitting electric resistivity of graphite foil in horizontal contacts. Specifically, temperature dependencies of thermal conductivity (in horizontal and vertical contacts) and electric resistivity (in vertical contacts) were fitted by assuming these parameters were proportional or inversely proportional to the temperature dependency of graphite foil electric resistivity in horizontal contacts.

In the above-cited studies, quantitative comparisons with experimental data are limited and model reliability was not tested by comparing experimental data with model predictions. In particular, temperature-controlled runs are usually considered, thus complicating modeling activity with the introduction of additional adjustable parameters for the mathematical description of the control system. Typically, quantitative comparisons with experimental data are provided in terms of temperature only, without considering voltage and displacement.

In our view, on the other hand, a reliable model of SPS can be obtained by separately analyzing the increasingly complex system behavior within the framework of a step-by-step procedure, where physicochemical phenomena, previously excluded, are gradually introduced along with their unknown model parameters. This approach allows investigators to independently fit the complete set of unknown parameters of the comprehensive SPS model, thus avoiding the masking effect given by the various phenomena involved in the whole process. In this work, the first step of this ideal approach is carried out by taking into account heat transfer phenomena, current distribution, and stress–strain mechanics. First, a detailed analysis of SPS apparatus is performed from the perspective of electric phenomena by highlighting the importance of rms electric current and the inductive character of the system. In particular, evaluation of the predominant electric and thermal contact resistances is carried out by comparing model results with experimental data obtained when appropriate samples characterized by the absence of powders are used. Specifically, explicit dependency of horizontal electric and thermal contact resistances on applied load and local temperature is obtained.

Experimental

Experimental runs were performed on a model 515S SPS apparatus (Sumitomo Heavy Industries Ltd., Kanagawa, Japan). The power supply is a DC-pulse generator, which is reported to

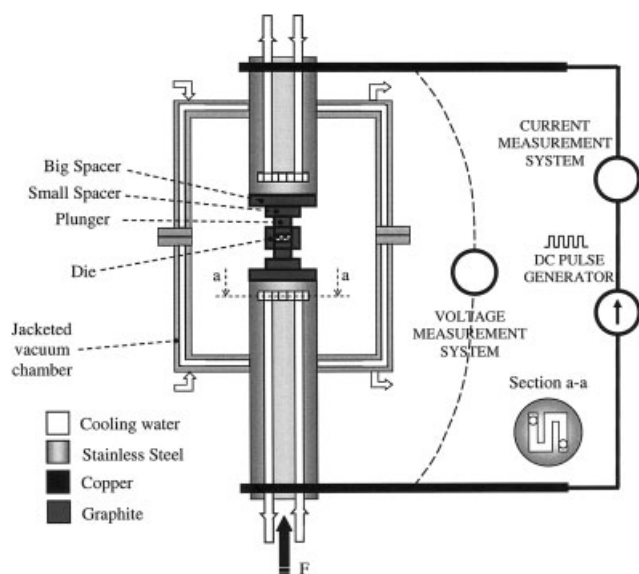


Figure 1. Schematic representation of SPS experimental setup (not to scale).

provide a maximum current and voltage equal to 1500 A and 10 V, respectively, whereas the mechanical load applied through the hydraulic system can be varied between 3 and 50 kN. Specifically, current pulses of 3.3-ms fixed duration are generated. The operator is free to select the pulse sequence, that is, number of ON pulses (from 1 to 99) vs. number of OFF pulses (from 1 to 9), representing periods of time with zero current. Typically, a 12/2 sequence is adopted (as prescribed by Sumitomo). This choice corresponds to the repetition of a sequence of 12 ON pulses followed by 2 OFF pulses for a total sequence period of 46.2 ms (that is, 3.3×14 ms). It should be mentioned that no specifications are available regarding the measured current and voltage, that is, average or rms values. In reference to Figure 1, the powder sample (when used) is inserted into a die placed between two plungers that are not in direct contact with the stainless steel rams, although spacers are typically inserted between them. With reference to electric phenomena, the end part of the rams are connected to an elec-

tric generator through copper bars and wires. Spacers, plungers, and die are made of AT101-grade graphite (ATAL SRL, Lecco, Italy), which guarantees relatively high electric and thermal conductivities, that is, lower power dissipation, higher heat transfer to powder specimen, and quicker cooling step. The use of graphite limits the attainable pressure level to a value <100 MPa, whereas the vacuum chamber disallows chemical oxidation of graphitic elements. As may be seen in Figure 1, the vacuum chamber consists of two coaxial cylinders both jacketed with cooling water circulation. A vacuum level down to 10 Pa is attainable with the SPS 515S model. Rams are made of stainless steel (AISI 304) and cooling water flows through them, as depicted in Figure 1, where the corresponding horizontal section a–a of the water circuit is also shown.

The SPS machine is typically provided with two classic PID control loops for temperature and mechanical load control, which act on the electric current and hydraulic systems, respectively. Temperature can be measured by means of a pyrometer focused on die surface or using a thermocouple system. Mechanical load is measured by means of a load cell. A linear encoder measures displacement at the bottom end of the lower ram where the vertical mechanical load is applied, whereas the top end of the upper ram is blocked in a fixed vertical position.

Thus, from an operational perspective (cf. Figure 2), once the system geometry (that is, sizes of sample, die, plungers, and spacers) is chosen along with the pulse cycle, and the temperature and mechanical load profiles to be tracked are set, the SPS automatically adjusts (that is, closed control loops) the electric current and oil pressure of the hydraulic system during the experimental run. Correspondingly, the force acting on the lower ram, the current, and the voltage attained across the system as a function of its electric load are measured. Alternatively, control loops can be opened. In this case, the operator manually sets electric current and the desired initial level of applied mechanical load, which is determined by the oil pressure of the hydraulic system. It is worth noting that, as a result of thermal expansion and sintering phenomena, the actual level of applied force undergoes small changes (maximum variation is roughly 10%), so that it is usually considered a “constant value” when specifying the operative conditions. If the mechanical-load control loop is closed, the temperature control loop must also be closed in the

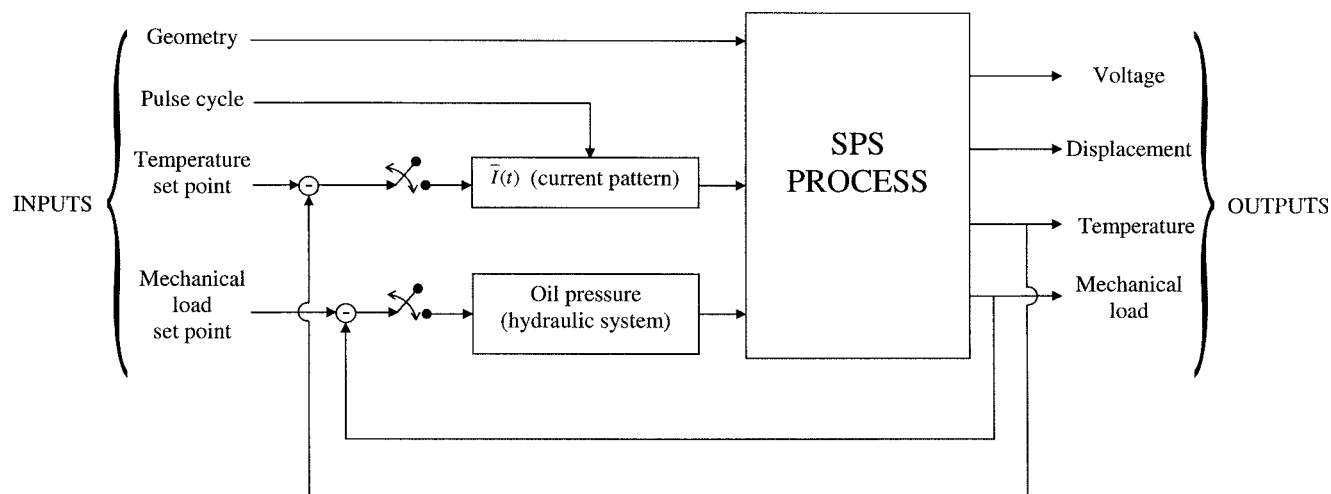
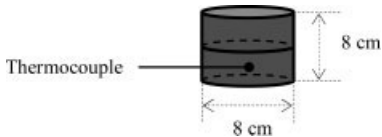
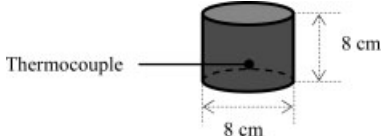
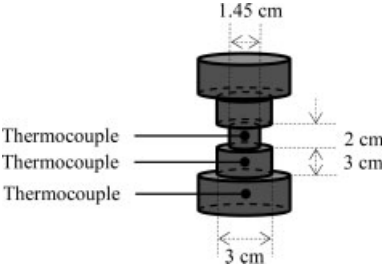
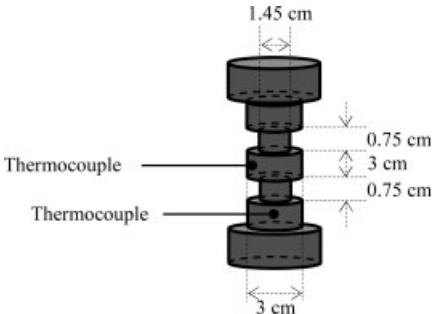
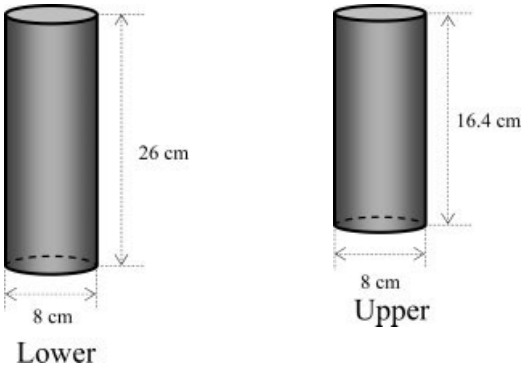


Figure 2. Input/Output scheme of SPS process.

Table 1. Sample Configurations and Dimensions (Not to Scale) of Graphite and Stainless Steel Elements of the SPS System Investigated

Sample	Element	Dimensions
I	Two big spacers	
II		
III	Two big spacers + two small spacers + one plunger	
IV	Two big spacers + two small spacers + one monolithic die and plungers ensemble	
	Electrodes	

SPS 515S model. In this work, experimental runs are performed with opened control loops, so that PID feedback controls are not considered in the numerical simulations, accordingly.

With respect to evaluation of electric quantities, we found that SPS 515S model is typically available as equipped with a measuring system that provides the average value of current [that is, $\bar{I} = (1/\tau) \int_t^{t+\tau} I(t)dt$] flowing in the circuit and the average value of voltage [that is, $\bar{V} = (1/\tau) \int_t^{t+\tau} V(t)dt$]. However, such average values are not appropriate to determine heating because of the Joule effect in SPS processes. Indeed, it is well known that resistive heating occurring in a pulsed-DC–

driven electric circuit is proportional to the rms value of flowing current [that is, $I_{rms} = (1/\tau) \int_t^{t+\tau} I^2(t)dt$].¹³ For this reason, a new data acquisition system was designed and installed to independently measure instantaneous (pulsed) values of electric current and voltage, from which average and rms values are calculated. In particular, with reference to Figure 1, an open-loop Hall effect current transducer was used (HAX 2500-S, nominal primary current 2500 A rms, maximum primary current 5500 A, bandwidth 25 kHz, accuracy 1% at nominal current; LEM, Geneva, Switzerland) along with a voltage isolation amplifier (DSCA41-09, input range –40 to +40 V,

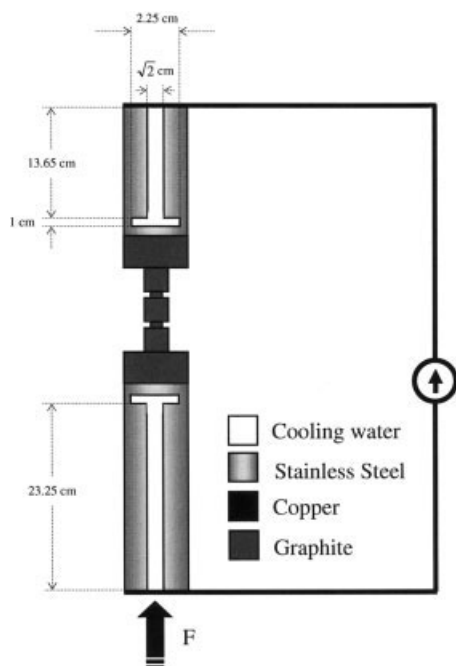


Figure 3. Idealized SPS system configuration for 2D model simulation (not to scale).

bandwidth 3 kHz, accuracy 0.03% of full scale; Dataforth Corp., Tucson, AZ). The latter apparatus is connected to the copper bars closest to the stainless steel electrodes. The output signals of these transducers are fed to a data acquisition board (200 kS/s, 12-bit, 16 Analog Input Multifunction; National Instruments, Austin, TX) connected to a PC, where a specifically designed LabVIEW (National Instruments) virtual instrument is installed. This data acquisition system is able to instantaneously collect current and voltage measurements and calculate the corresponding average and rms values (sampling time $\tau = 0.5$ s), along with all the other variables typically

measured in SPS processes (that is, time, temperature, displacement, load, and gas pressure).

Specific sample configurations characterized by the absence of powders are considered in this work. In particular, we used the graphite cylindrical samples reported in Table 1, along with the size of upper and lower stainless steel electrodes provided with the SPS 515S model. Graphite samples were inserted between rams during experimental runs. It should be noted that sample IV consists of two large spacers, two small spacers, and one monolithic block (to avoid vertical contact resistances), mimicking two plungers slid into a die.

Description of the Model

Because of heat losses by radiation from lateral surfaces as well as heat removal by cooling water in the axial direction, along with variations of cross sections, a two-dimensional (2D) model for the heat balance of SPS technique is proposed, whereas radial symmetry is assumed. Vertical symmetry cannot be assumed because of the different heights of stainless steel electrodes and the corresponding cooling circuits. Although isotropic materials are considered, temperature variations in both the radial and the axial directions induce spatial gradients of thermophysical properties such as electric and thermal conductivities and coefficient of thermal expansion. In what follows, a 2D energy balance accompanied by a quantitative description of the electric and mechanical behavior of SPS apparatus depicted in Figure 1 are reported.

The energy balance in cylindrical coordinates (r, z) related to both the stainless steel rams and the graphite samples shown in Figure 3 and Table 1 is given by the following equation:

$$\rho_i C_{p,i} \frac{\partial T}{\partial t} = \frac{1}{r} \frac{\partial}{\partial r} \left(r k_i \frac{\partial T}{\partial r} \right) + \frac{\partial}{\partial z} \left(k_i \frac{\partial T}{\partial z} \right) + \frac{1}{\rho_{el,i}} \left[\left(\frac{\partial \varphi}{\partial r} \right)^2 + \left(\frac{\partial \varphi}{\partial z} \right)^2 \right]$$

$$i = \begin{cases} \text{Stainless Steel} \\ \text{Graphite} \end{cases} \quad (1)$$

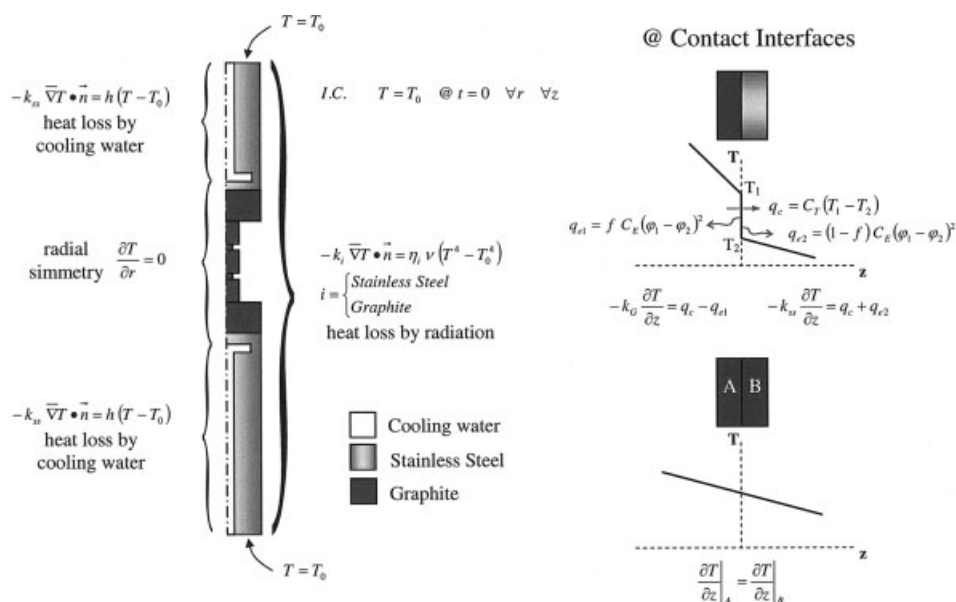


Figure 4. Initial and boundary conditions for the energy balance equation (not to scale).

where T indicates temperature and φ represents the resistive portion of rms voltage, as will be clarified later. Temperature dependencies of the thermophysical parameters C_p (heat capacity), k (thermal conductivity), and ρ_{el} (electric resistivity) are taken into account, as will be shown later.

Initial and boundary conditions are given in Figure 4. In particular, \vec{n} represents the surface unit vector (perpendicular and outward); C_T and C_E are the thermal and electric contact conductances, respectively; meanings of the other symbols are listed below in the Notation section.

Only contact resistances at stainless steel–graphite interfaces are considered, with a local Joule heat (q_e) arising from electric contact resistance,¹¹ which has been equally split between the materials at the interface (that is, $f = 0.5$ is considered when solving the model).

It should be noted that the real configuration of the cooling water circuit inside stainless steel electrodes (cf. Figure 1) is potentially able to negate the assumption of radial symmetry, although it may still be reasonably adopted by taking into account the relatively high thermal conductivity of stainless steel. In this case, a hypothetical cooling circuit, where water is maintained at ambient temperature, is considered, as schematically shown in Figure 3. It is assumed that the heat flow rate in the real cooling system resulting from forced convection of cooling water is equivalent to the corresponding value of that shown in Figure 3, so that

$$(hS)_{\text{hypothetical cooling circuit}} = (hS)_{\text{real cooling circuit}} \quad (2)$$

From the knowledge of $(hS)_{\text{real cooling circuit}}$, by choosing a geometry of the hypothetical cooling system and consequently determining $(S)_{\text{hypothetical cooling circuit}}$, it follows that $(h)_{\text{hypothetical cooling circuit}}$ may be readily calculated from Eq. 2. It is worth noting that $(h)_{\text{real cooling circuit}}$ is predicted by means of typical correlations for forced convection in closed ducts (i.d. 1 cm; water flow rate experimentally evaluated equal to $5.5 \times 10^{-5} \text{ m}^3/\text{s}$).¹⁴ Referring to Figure 3, $(S)_{\text{hypothetical cooling circuit}}$ is evaluated by maintaining the same length of the real system, whereas the diameter of the hypothetical cooling system is determined to guarantee an equal overall Joule effect in

the two configurations (that is, equal electrode cross section available for electric current).

In principle, SPS systems involve time-varying electromagnetic fields for which the assumption of current density conservation, typically adopted in the literature,^{8,9,11} is not satisfied.¹³ Thus, to properly take into account magnetic induction and the corresponding Joule heat distribution, a more complex version of Maxwell's equations should be considered. Moreover, the entire model should be solved in the timescale of the generated electric pulses (fractions of a millisecond), whereas temperature and displacement change in a much larger timescale (that is, seconds at least). Clearly, such a mathematical description would be characterized by a high degree of stiffness and time-consuming solution.

Therefore, to develop a relatively simple but still adequate model of the SPS electromagnetic field, our strategy is to infer the so-called field theory model from analysis of the related electric circuit (that is, circuit theory model), by taking advantage of the measured macroscopic variables: instantaneous total current flowing inside the SPS system and voltage across the investigated portion of the electric circuit loop. To this aim, it is assumed that SPS behavior can be described through a nonideal inductor, that is, a resistance (R)–inductance (L) series combination, for which the following relationship holds:

$$V = V_R + V_L = RI + L \frac{dI}{dt} \quad (3)$$

where V and I represent the instantaneous voltage and electric current, respectively. According to Fano et al.,¹³ this approach allows one to consider a steady-state conduction model inside the conductor and a steady-state magnetic model outside the conductor. Therefore, the following steady-state conduction model,

$$\frac{1}{r} \frac{\partial}{\partial r} \left(\frac{1}{\rho_{el,i}} r \frac{\partial \varphi}{\partial r} \right) + \frac{\partial}{\partial z} \left(\frac{1}{\rho_{el,i}} \frac{\partial \varphi}{\partial z} \right) = 0 \quad (4)$$

$$i = \begin{cases} \text{Stainless Steel} \\ \text{Graphite} \end{cases}$$

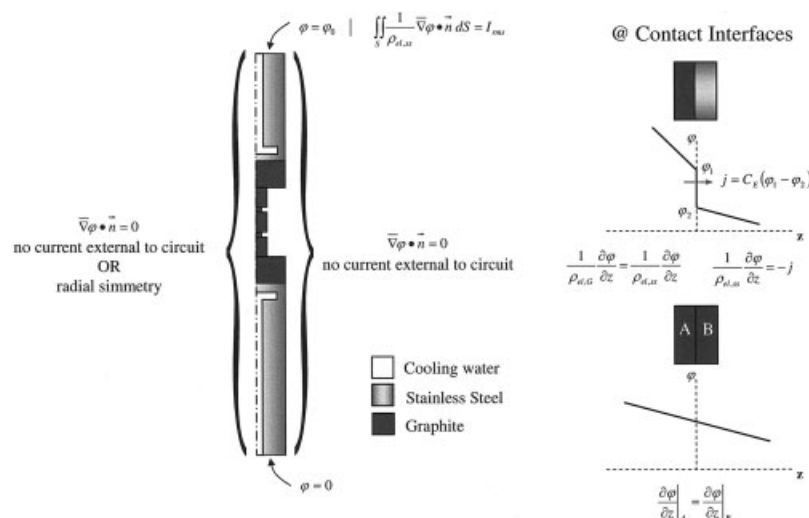


Figure 5. Boundary conditions for the steady-state electric conduction model equation (not to scale).

coupled with the boundary conditions given in Figure 5, can still be adequately adopted to describe the electrical behavior inside the conductor of the SPS system. Only contact resistances at stainless steel–graphite interfaces are considered, whereas equipotential conditions for electrode surfaces in contact with copper bars (cf. Figure 1) have been adopted.

It is then apparent that a method for obtaining the experimental counterpart of the resistive portion of the rms voltage (φ) from the instantaneously measured voltage and current needs to be developed. To this aim, the following Fourier series development of pulsed direct current,

$$I = a_0 + \sum_{n=1}^{\infty} [a_n \cos(w_n t) + b_n \sin(w_n t)]$$

$$w_n = \frac{2\pi n}{\tau} = 2\pi f_n = n\omega_l \quad (5)$$

can be substituted into Eq. 3. Thus, the average and rms expressions for voltage and electric current along with the average power dissipated (\bar{P}) are evaluated as follows:

$$\bar{I} = a_0 \quad \bar{V} = R\bar{I} \quad I_{RMS} = \sqrt{a_0^2 + \sum_{n=1}^{\infty} \left(\frac{a_n^2 + b_n^2}{2} \right)}$$

$$V_{RMS} = \sqrt{R^2 + X_L^2} I_{RMS} \quad \bar{P} = R I_{RMS}^2 \quad (6)$$

where X_L represents the inductive reactance

$$X_L = \sqrt{w_l^2 L^2 \left\{ \frac{\sum_{n=1}^{\infty} \left[\frac{n^2(a_n^2 + b_n^2)}{2} \right]}{a_0^2 + \sum_{n=1}^{\infty} \left[\frac{(a_n^2 + b_n^2)}{2} \right]} \right\}}$$

From the Eq. 6 system, it can be seen that the experimental value of voltage to be compared with the steady-state conduction model output (where I_{rms} is the forcing function) is represented by $\varphi = R I_{rms}$, where resistance is determined from the measured average voltage and electric current ($R = \bar{V}/\bar{I}$).

By considering graphite and stainless steel elements as elastic bodies subjected to a mechanical and thermal load, the mechanical behavior of SPS systems can be simulated by the following pseudostatic equilibrium model:

$$\left. \begin{aligned} \frac{\partial \tau_{zr}}{\partial r} + \frac{1}{r} \sigma_r + \frac{\partial \sigma_r}{\partial r} &= 0 & \frac{\partial \sigma_z}{\partial z} + \frac{1}{r} \tau_{zr} \frac{\partial \tau_{zr}}{\partial r} &= 0 \\ \varepsilon_r &= \frac{1}{E_i} (\sigma_r - \nu_i \sigma_z) + \alpha_i (T - T_0) = \frac{\partial u_r}{\partial r} \\ \varepsilon_z &= \frac{1}{E_i} (\sigma_z - \nu_i \sigma_r) + \alpha_i (T - T_0) = \frac{\partial u_z}{\partial z} \\ \gamma_{zr} &= 2 \left(\frac{1 + \nu_i}{E_i} \right) \tau_{zr} = \left(\frac{\partial u_r}{\partial z} + \frac{\partial u_z}{\partial r} \right) \end{aligned} \right\} i = \begin{cases} \text{Stainless Steel} \\ \text{Graphite} \end{cases} \quad (7)$$

where σ_r , σ_z , and τ_{zr} are the 2D components of the stress tensor; ε_r , ε_z , and γ_{zr} are the corresponding components of the strain tensor; u_r and u_z are the radial and axial displacements; and E , ν , and α are the Young's modulus, Poisson's ratio, and the coefficient of thermal expansion, respectively. Suffix i indicates that the Eq. 7 system is valid for both graphite and

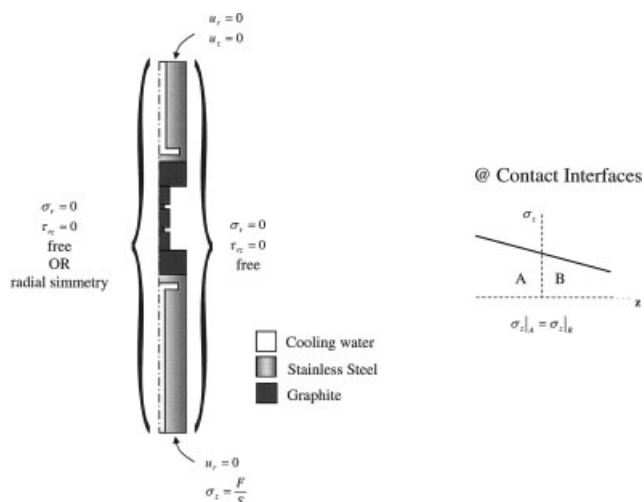


Figure 6. Boundary conditions for the pseudostatic equilibrium model equation (not to scale).

stainless steel elements, provided that the corresponding thermophysical parameters are properly considered. Boundary conditions for the mechanical model of the SPS system are given in Figure 6. In this case, ideal contact (that is, no friction) at interfaces between different elements is considered.

From a mathematical perspective, the preceding model is not fully coupled with temperature and electric current distribution. Indeed, once thermal and electric current balances are solved, temperature distribution represents the input for the mechanical model that allows one to determine the stress–strain distribution and the displacement temporal profile. Actually, the implicit assumption adopted (that is, the spatial domain of integration does not change substantially as a result of thermal expansion and mechanical load), however, is reasonable for the SPS systems modeled in this work. Indeed, the order of magnitude of the resulting negative displacement arising from thermal expansion is equal to 10^{-3} m, whereas the height of the apparatus is 1 m. Of course, it is also implicitly assumed that the contribution to both thermal expansion and mechanical load is equally distributed between the different elements comprising the stainless steel electrodes. On the other hand, such an assumption may be not valid when modeling SPS system behavior in the presence of powder samples, where a positive displacement with order of magnitude of about $3\text{--}5 \times 10^{-3}$ m is basically localized in the shrinking powder specimen. Modeling with moving boundaries should be considered in this case, especially if spatiotemporal profiles of final product density are simulated.

The system of differential–algebraic–integral equations described earlier has been solved by the finite-element method (FEM) numerical technique. In particular, the commercial software Multiphysics™ 3.2 (COMSOL, Inc., Stockholm, Sweden) has been adopted (degrees of freedom and number of elements are about 25,000 and 3000, respectively). Parameters used for computations are reported in Table 2 and Figures 7 and 8. In particular, the heat-transfer coefficient (h) is calculated as discussed above; determination of heat graphite thermal conductivity deserves a comment, however, because different data are reported in the literature. In this work, $k_G(T)$ is evaluated by averaging the temperature dependencies given by

Table 2. Model Parameters

Parameter	Value	Reference(s)
$C_{p,G}$	See Figure 7	15
$C_{p,ss}$	See Figure 8	16
E_G	$1.1 \cdot 10^4$ (N mm ⁻²)	ATAL vendor
E_{ss}	$19.3 \cdot 10^4$ (N mm ⁻²)	17
f	0.5	11
h	4725 (W m ⁻² K ⁻¹)	This work
H_G	$3.5 \cdot 10^9$ (Pa)	ATAL vendor
H_{ss}	$1.92 \cdot 10^9$ (Pa)	18
k_G	See Figure 7	ATAL vendor; 16; 19
k_{ss}	See Figure 8	20
α_G	See Figure 7	21
α_{ss}	See Figure 8	17
η_G	0.85	6; 8; 9; 11
η_{ss}	0.4	22
ν	$5.67 \cdot 10^{-8}$ (W m ⁻² K ⁻⁴)	23
ρ_G	1750 (kg m ⁻³)	ATAL vendor
ρ_{ss}	8000 (kg m ⁻³)	16
$\rho_{el,G}$	See Figure 7	ATAL vendor
$\rho_{el,ss}$	See Figure 8	16
ν_G	0.33	This work
ν_{ss}	0.29	17

the two different references available in the literature consistent with the only value ($100 \text{ W m}^{-1} \text{ }^\circ\text{C}^{-1}$ at 25°C) provided by the ATAL vendor for graphite AT101. The only unknown model parameters that remain are thus thermal and electric conductances, C_T and C_E , at the horizontal contacts between stainless steel electrodes and graphite spacers (see boundary

conditions in Figures 4 and 5). Determination of the dependency of these two parameters on temperature and applied mechanical load is described in the next section.

Results and Discussion

In what follows, the results related to the experimental activity performed to support some of the modeling assumptions are reported first. Next, the comparison between experimental data and model results will be illustrated in terms of both the fitting procedure adopted to evaluate the unknown parameters and the prediction capability of the proposed SPS apparatus model.

Figure 9a shows the measured temporal profile of instantaneous current along with the corresponding calculated average and rms values, for a 12/2 pulse sequence. Obviously, current behavior is completely independent from the specific sample used because current is one of the forcing (INPUT) functions of SPS (cf. Figure 2), that is, current is a manipulated variable with respect to process control. If the ratio between the number of ON pulses to that of OFF pulses is decreased, while keeping constant the rms current, the DC-pulse generator provides fewer pulses with higher peaks. This aspect determines a lower average current, as indicated in Figure 9b. In addition, from the same figure, it is apparent that the ratio I_{rms}/\bar{I} tends asymptotically to 1 as I_{rms} increases (pulse cycles equal to 12/2 and 99/1, respectively). This behavior is explained by the fact that by increasing the current level, ON pulses of fixed

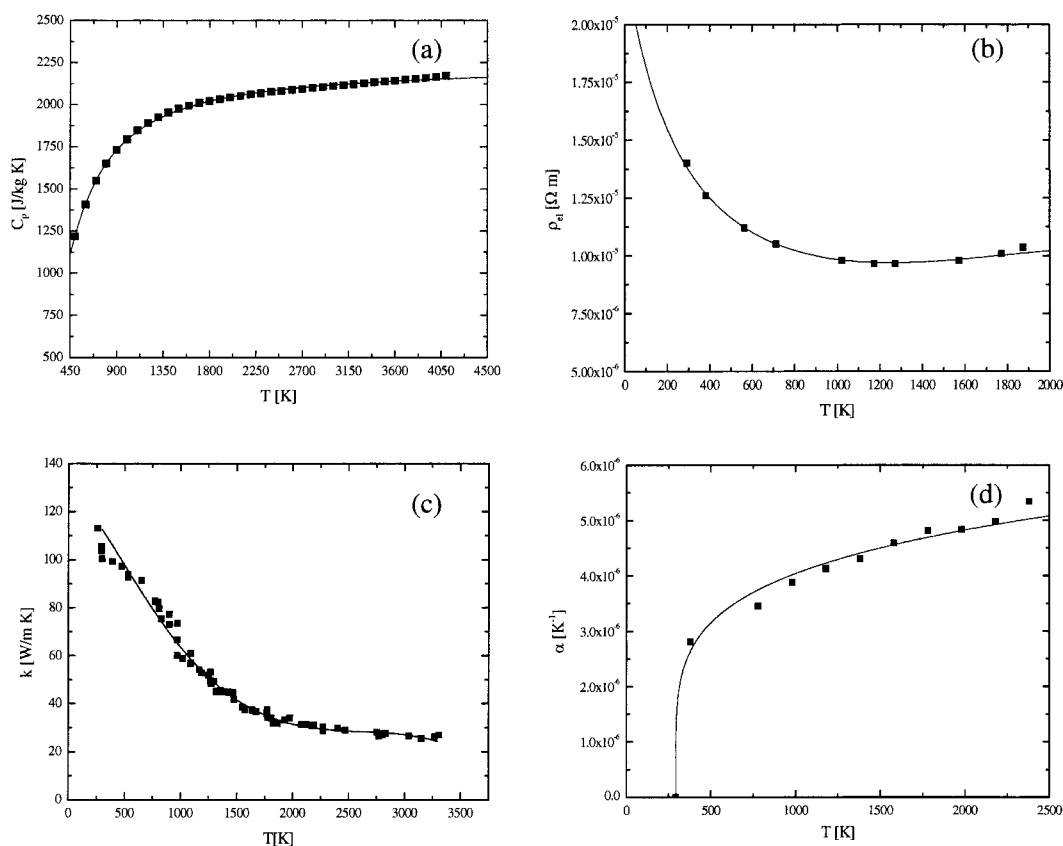


Figure 7. Thermophysical properties of AT 101 (ATAL) graphite.

Heat capacity (a), electrical resistivity (b), thermal conductivity (c), and coefficient of thermal expansion (d).

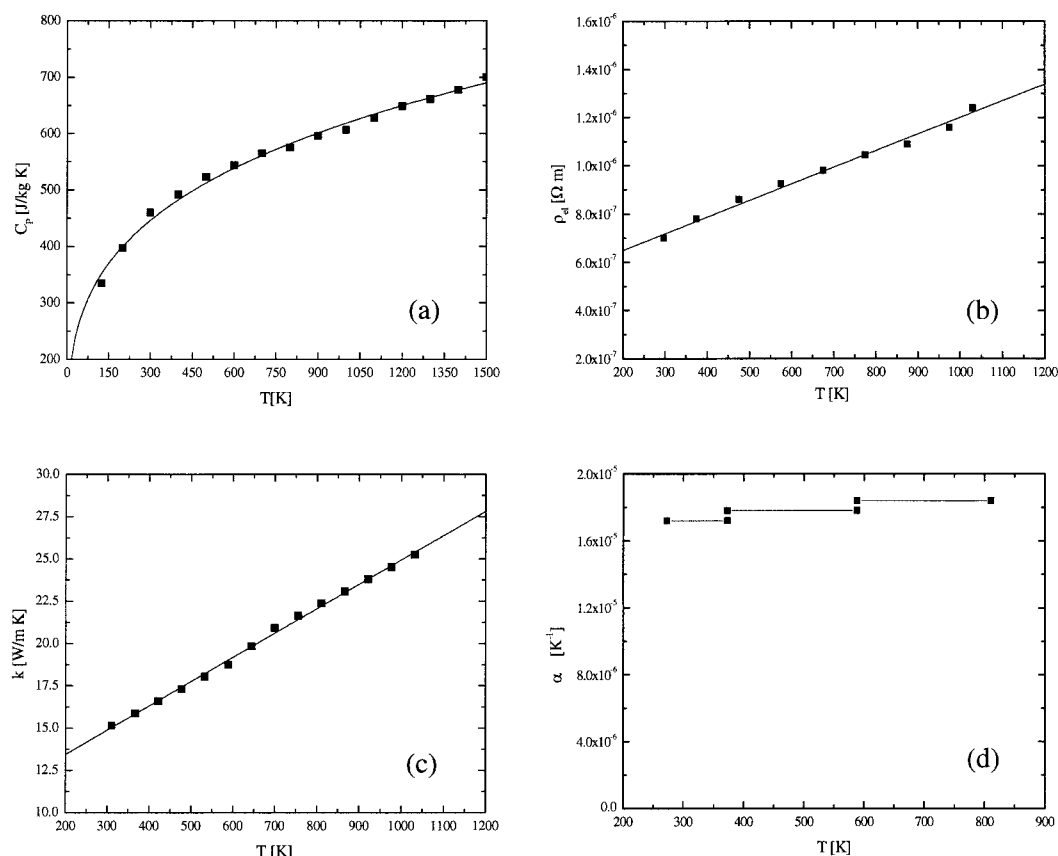


Figure 8. Thermophysical properties of AISI 304 stainless steel.

Heat capacity (a), electrical resistivity (b), thermal conductivity (c), and coefficient of thermal expansion (d).

duration (that is, 3.3 ms) tend to overlap, thus determining a more continuous temporal profile of instantaneous current. Thus, the ratio between the corresponding average and rms values is reduced. The same effect can be reached by increasing the ratio between numbers of ON and OFF pulses. In any event, from Figure 9b it is clearly seen that the average current \bar{I} can be significantly different from the corresponding rms

value as given by the power supply of the SPS 515S model, especially at relatively low current levels and/or low ratios between numbers of ON and OFF pulses. Therefore, it can be concluded that measurement of rms current is necessary for properly evaluating Joule heating or energy dissipation in the SPS system. Thus, what still needs to be verified is whether the knowledge of $I_{rms}(t)$ is not only necessary but also suffi-

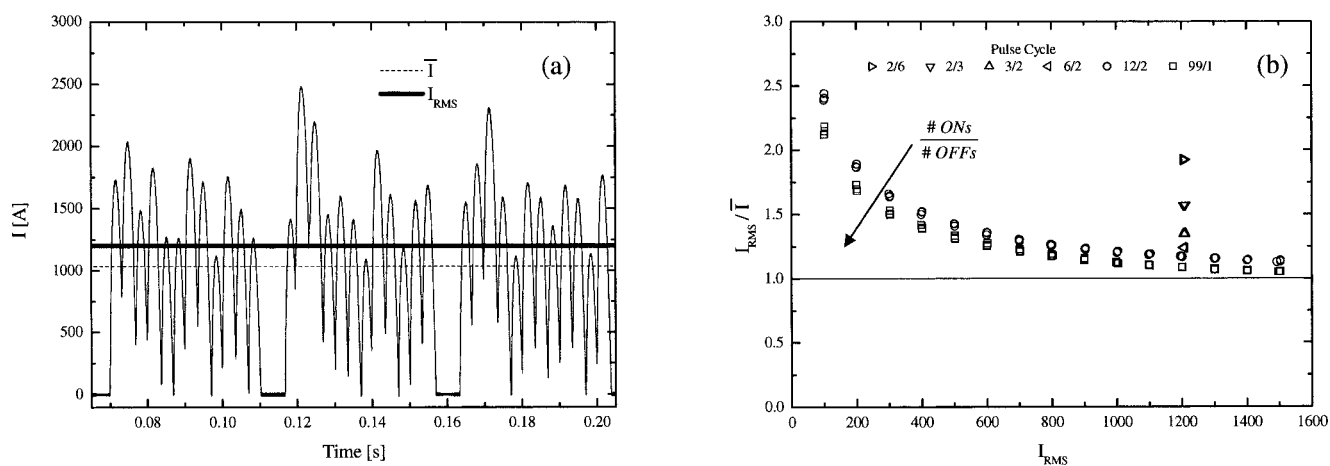


Figure 9. Instantaneous, average, and rms electric current temporal profiles when a 12/2 pulse cycle is adopted (a); effect of pulse cycle on I_{rms}/\bar{I} vs I_{rms} (b).

cient to describe the system behavior (that is, measured temporal profiles of temperature, voltage, and displacement), at least in the case of the absence of powders.

In the experimental results shown in Figure 10, where the case of sample I subjected to the rms electric current step of 1200 A for 20 min under an initial applied mechanical load of 3 kN is examined, it is shown that temperature, voltage, and displacement temporal profiles remain the same, independently of the specific pulse sequence adopted. This means that the rms value of electric current flowing into the SPS apparatus alone is responsible for system behavior because Joule heat is the unique effect provided by a pulsed DC flowing through a given SPS system without powders. Therefore, specifying the rms value of electric current is the necessary and sufficient condition for quantitatively describing SPS systems characterized by the absence of powders.

The temporal profiles of instantaneous electric current and voltage measured when sample I is subjected to rms current of 1200 A are plotted in Figure 11a. The “inductive” behavior of the system is clearly shown, given that voltage anticipates electric current. Of course, the inductive nature of the SPS system arises from the pulsing of the electric current forced to flow through the sample, which causes a pulsed flux of the related magnetic field, that is, self-inductance. This experimental evidence is further supported by the results shown in Figure 11b, where the ratio between rms and average voltage is plotted against the analogous ratio related to the current. From an electrical standpoint, if the SPS system behaves like an ideal resistor, these experimental data have to line up along the bisector shown in Figure 11b (cf. Eq. 6 system), although they do not. Actually, the inductive character of the SPS apparatus slightly depends on the chosen pulse sequence and, remarkably, on the level of electric current flowing inside the system. In fact, it follows that by increasing the rms electric current, the ratio I_{rms}/\bar{I} decreases (cf. Figure 9b) and V_{rms}/\bar{V} tends to I_{rms}/\bar{I} (cf. Figure 11b), that is, the inductive character of SPS is reduced. This behavior can be explained by the same argument raised above, that is, an increasing current level produces a more continuous instantaneous current temporal profile, which in turn determines a less inductive character.

Figure 12 shows the fast Fourier transforms (FFT) of the pulsed electrical current depicted in Figure 9a, in terms of amplitude and phase (Figure 12a) or power (that is, square of amplitude) and phase (Figure 12b). These plots allow us to determine the relevant contribution of the different harmonics to a Fourier series development of the pulsed current. Apart from the DC component at zero frequency, the most significant higher harmonics are too low (maximum 300 Hz) to cause the skin effect in the graphite and stainless steel elements whose sizes are reported in Table 1.⁹ This suggests that the observed inductive behavior of the system does not arise from the differences of magnetic flux linked by the concentric filaments that “internally” form the cross section of graphite and stainless steel elements (that is, the skin effect).²⁴ Presumably, this inductive behavior arises from the temporal variation of magnetic flux linked to the surface delimited by the “external” electric circuit loop in the SPS system (see Figure 1). Such a contribution can be adequately simulated by considering Eq. 3. This is confirmed in Figure 13, where we report the comparison between experimentally measured voltage (as shown in Figure 11a) and that calculated by means of Eq. 3 on the basis of the

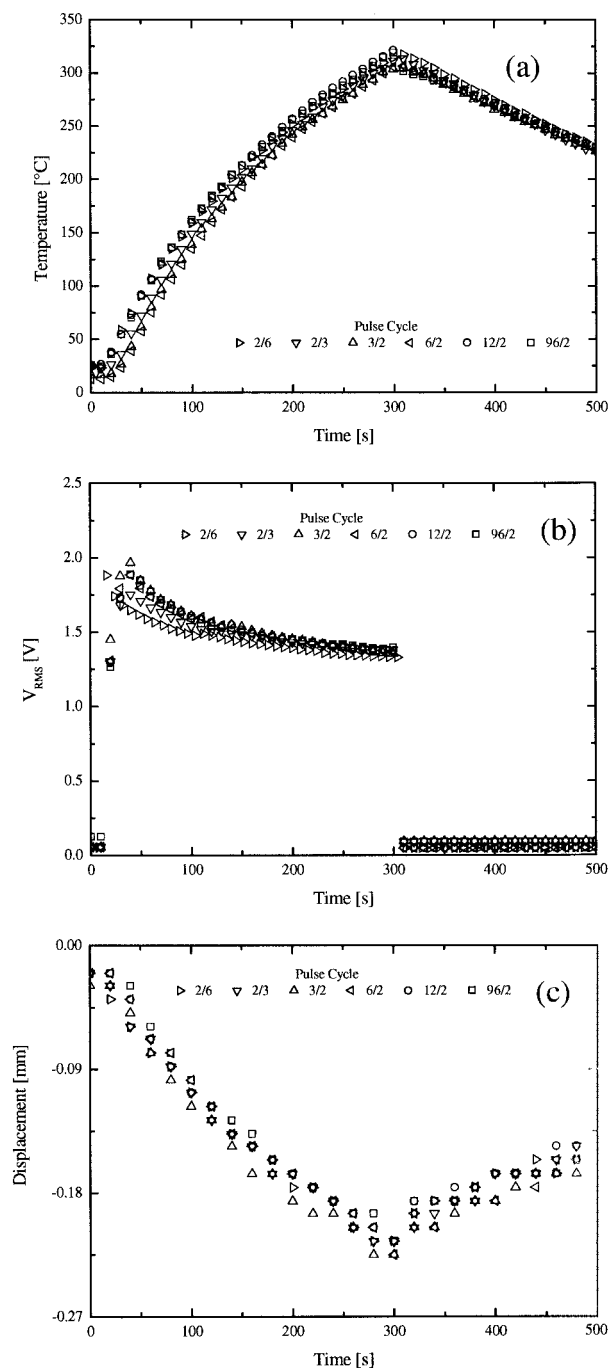


Figure 10. Temporal profiles of temperature (a) taken at the center of the lower big spacer ($r = 0$, $z = 28$ cm), rms voltage (b), and displacement (c), when sample I is submitted to rms electric current step of 1200 A for 20 min, with an initial load of 3 kN.

corresponding electric current. Note that R and L have been evaluated by fitting the experimental data: the corresponding values are $6.74 \times 10^{-4} \Omega$ and $5.0 \times 10^{-7} \text{ H}$, respectively. Thus, SPS system behavior can be properly described through a nonideal inductor, that is, a resistance (R)–inductance (L) series combination, as assumed in the modeling section.

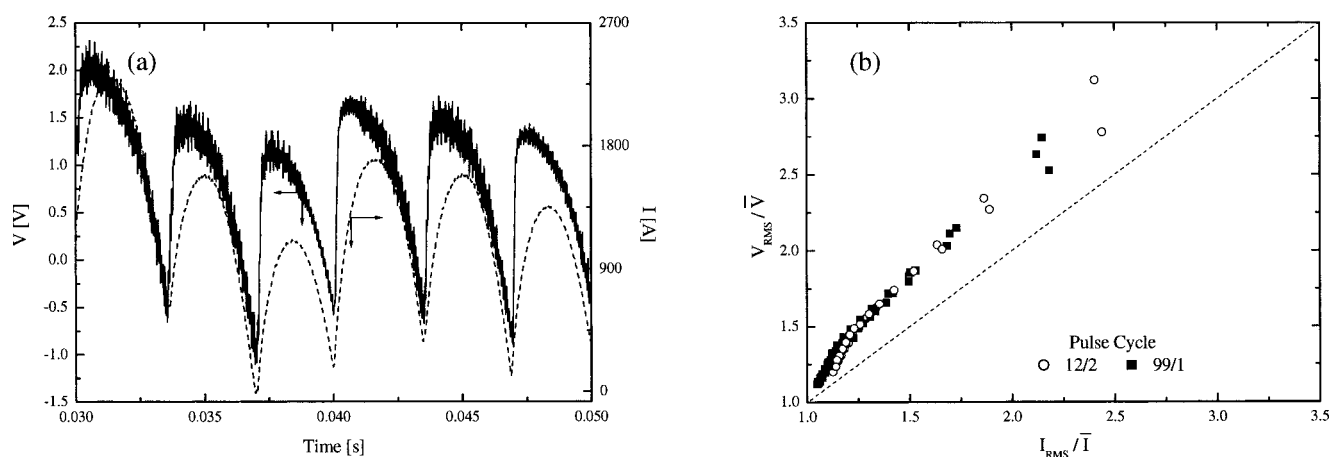


Figure 11. Instantaneous voltage and current with a 12/2 pulse cycle (a); V_{rms}/\bar{V} vs. I_{rms}/\bar{I} measured when using sample I with a load of 3 kN (b).

It is worth pointing out that this magnetic induction is not always relevant in SPS systems. In principle, every material that takes part in an electric circuit shows resistive, inductive, and capacitive behavior, all of which may influence circuit reactances. The relative importance of each contribution depends on element size. In particular, the choice of sample I enhances the inductive character with respect to the resistive one, whereas in samples III or IV, where cross sections for electric current flowing are smaller, the effect of induction phenomena becomes negligible.

Figure 14 shows the direct comparison between temperature and voltage temporal profiles when sample I and sample II are used under the same operating conditions, that is, a rectangular profile of rms current (amplitude 1200 A, 35-min duration) at 12/2 pulse sequence and an initial mechanical load equal to 3 kN. It clearly follows that horizontal contact resistances between graphite elements can be neglected. Figure 15 shows the same comparison when a graphite foil (0.13 mm thick; Alfa Aesar GmbH, Karlsruhe, Germany) is inserted at the contacts of sample I with stainless steel electrodes. The experimental runs are repeated several times as shown in Figures 14

and 15 to appreciate the reproducibility obtainable with SPS systems. Because significant differences are found in terms of both temperature and voltage temporal profiles, it is apparent that both thermal and electric contact resistances between graphite and stainless steel elements need to be taken into account. Indeed, according to Madhusadana,²⁵ conducting interstitial or filler material inserted in the gaps left by actual solid–solid point contact increases the real surface of contact between interfacing elements, thus reducing constriction resistances. Therefore, in our case the presence of graphite foil reduces the relevant horizontal contact resistances, so that lower temperature and voltage temporal profiles are obtained. Presumably, machined graphite parts used in this work possess a lower surface roughness than that of stainless steel electrodes provided with the SPS 515S model. It is worth noting that, to experimentally highlight the presence of thermal and electric contact resistances in the horizontal position, the lowest applicable mechanical load and the higher nominal contact surface among the available samples (see Table 1) have been used.

From the results reported earlier, the validity of some of the key assumptions made when developing the proposed SPS

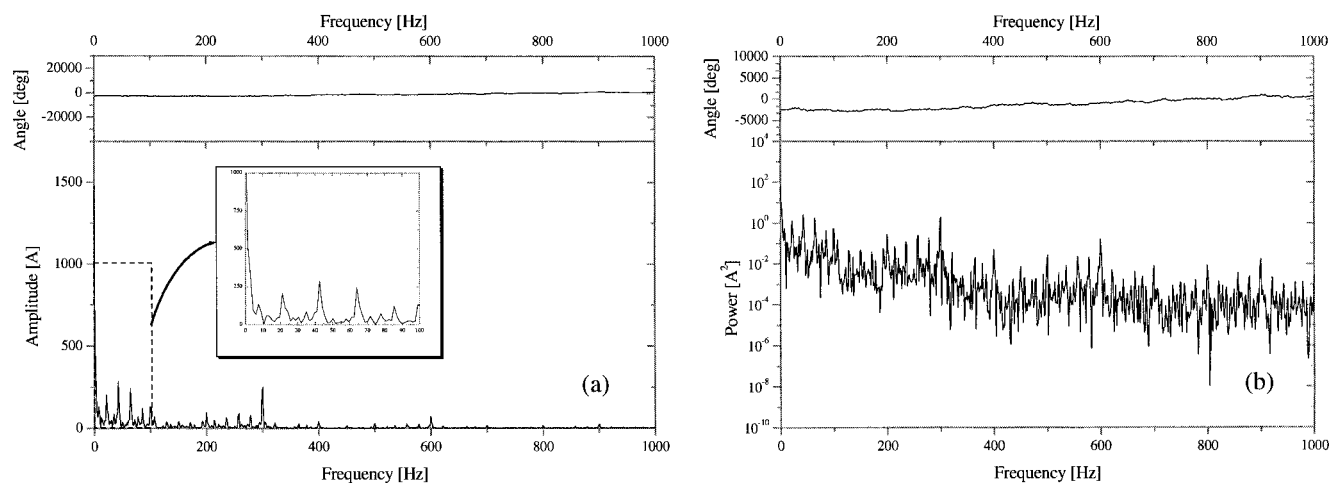


Figure 12. FFT in terms of amplitude and phase (a) and power and phase (b) vs. frequency of the instantaneous current reported in Figure 9a.

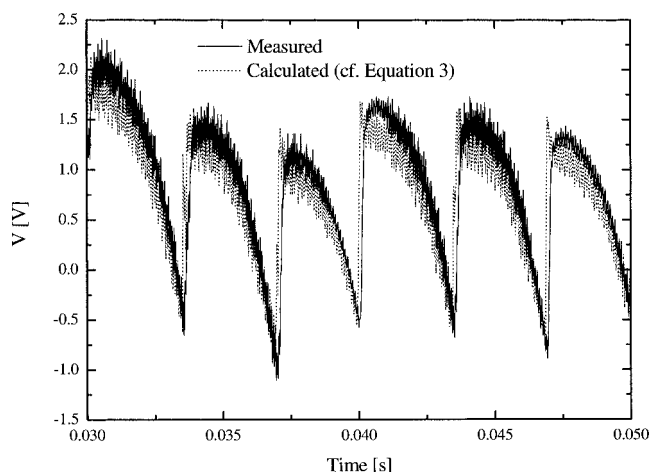


Figure 13. Comparison between temporal profiles of the measured instantaneous voltage and that calculated by means of Eq. 3 using the corresponding measurement of instantaneous electric current (cf. Figure 11a).

model are clearly demonstrated. The fitting procedure adopted to evaluate the unknown model parameters will now be described and discussed.

According to Madhusadana and Babu et al.,^{25,26} thermal and electric constriction conductances are related to temperature and applied mechanical load as follows:

$$C_T(T, P) = \alpha_T k_{Harm} \left(\frac{P}{H_{Harm}} \right)^{\beta_T} \quad (8)$$

$$C_E(T, P) = \alpha_E \sigma_{el, Harm} \left(\frac{P}{H_{Harm}} \right)^{\beta_E} \quad (9)$$

where $P (=F/S)$ represents the mechanical pressure uniformly applied at the contact surface area (S) between graphite and

stainless steel. The parameters k_{Harm} and $\sigma_{el, Harm}$, which take into account the temperature dependency of contact conductances, are expressed as follows using the harmonic mean of the individual thermal and electric conductivities of graphite and stainless steel:

$$k_{Harm}(T) = \frac{2k_G(T)k_{ss}(T)}{k_G(T) + k_{ss}(T)} \quad (10)$$

$$\sigma_{el, Harm}(T) = \frac{2\sigma_{el, G}(T)\sigma_{el, ss}(T)}{\sigma_{el, G}(T) + \sigma_{el, ss}(T)} \quad (11)$$

Basically, the use of harmonic mean is a consequence of the series combination of the two interfacing materials that characterize the real contact. Analogously, in this work the parameter H_{Harm} is the harmonic mean between the hardnesses of graphite and stainless steel:

$$H_{Harm} = \frac{2H_G H_{ss}}{H_G + H_{ss}} \quad (12)$$

The remaining parameters appearing in Eqs. 8 and 9 (that is, α_T , β_T , α_E , and β_E) are the only adjustable variables in our model. They depend on surface roughness and plastic behavior of contact between graphite and stainless steel interfaces. These four parameters have been fitted by direct comparison between modeling results and experimental data in terms of temporal profiles of the resistive portion of rms voltage measured between electrodes' ends (φ_0) and temperature measured by a thermocouple placed in the axial position inside sample I, as depicted in Table 1. In particular, experimental runs conducted under applied initial mechanical loads in the range 3–50 kN, at a constant I_{rms} of 1200 A at 12/2 pulse cycle, have been performed. Experimental data for the case of 3, 20, and 50 kN are compared with modeling results in Figures 16a and 16b, 17a and 17b, and 18a and 18b, respectively, whereas fitted parameters are reported in Table 3 along with the 95% confidence band and correlation coefficient.

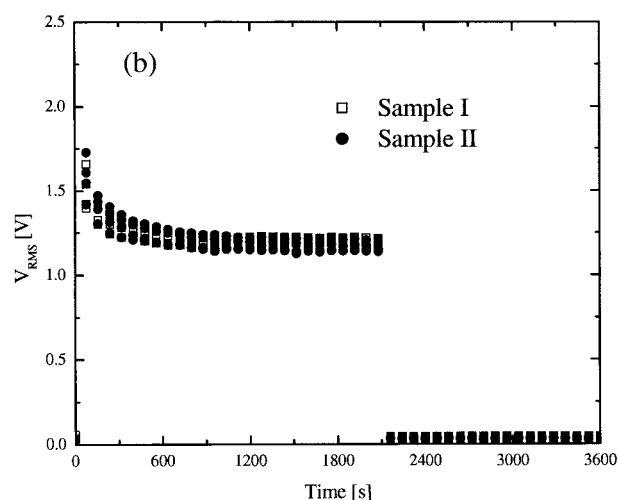
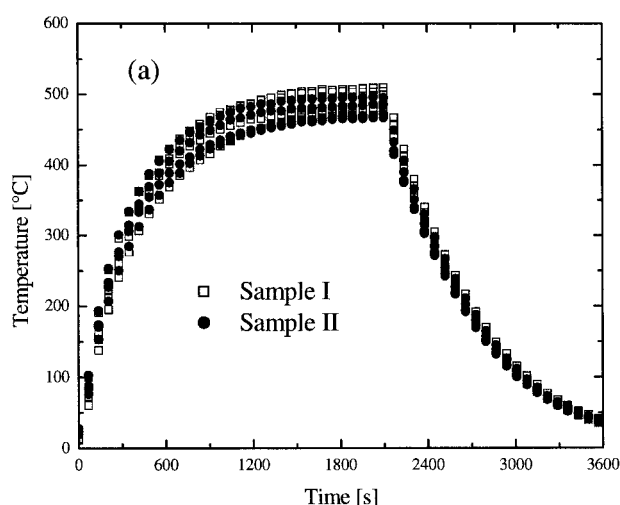


Figure 14. Comparison between sample I and sample II with respect to temporal profiles of measured temperature ($r = 0$, $z = 28$ cm) (a) and rms voltage (b), when rms current step of 1200 A is applied for 35 min with an initial load of 3 kN.

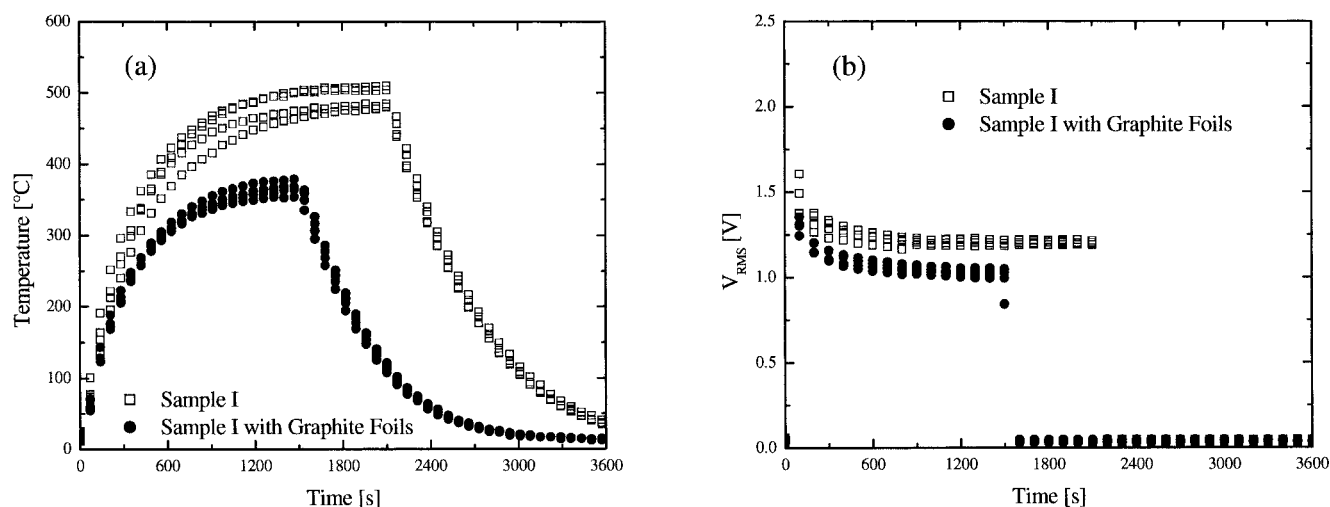


Figure 15. Comparison between sample I with and without graphite foils at stainless steel/graphite interfaces with respect to temporal profiles of measured temperature ($r = 0$, $z = 28$ cm) (a) and rms voltage (b), when rms current step of 1200 A is applied for 35 and 25 min, respectively, with an initial load of 3 kN.

icients. The corresponding values of electric and thermal conductances obtained in the range of temperature and mechanical load investigated in this work are $0.25 \div 1.7 \times 10^6 \Omega^{-1} \text{ m}^{-2}$ and $0.007 \div 2 \times 10^3 \text{ W m}^{-2} \text{ K}^{-1}$, respectively. It is worth noting that constant values for electric and thermal contact conductances in the horizontal position— $1.25 \times 10^7 \Omega^{-1} \text{ m}^{-2}$ and $2.4 \times 10^3 \text{ W m}^{-2} \text{ K}^{-1}$, respectively—were obtained by Zavaliangos et al.¹¹ These discrepancies may be ascribed to the fact that Zavaliangos et al.¹¹ considered the electrodes made of graphite (instead of stainless steel), whose thermophysical properties are rather different from those used in the present report. In Figures 16c, 17c, and 18c the corresponding displacement temporal profiles are also compared with the experimental results. Importantly, displacement arising from thermal expansion is completely predicted by the proposed model. A satisfactory simulation of the SPS system behavior in terms of temperature, voltage, and displacement is obtained, especially at higher applied mechanical loads, when temperature and voltage decrease as a result of lower contact resistances.

The importance of taking into account thermal and electric contact resistances when addressing quantitative modeling of the SPS system is further assessed in Figure 19. Here, the axial ($r = 3$ cm) profiles of temperature and the resistive portion of rms voltage at 1200 s (that is, just before the end of holding step) are reported for the case of 50 kN load (cf. Figure 18). It is apparent that significant changes of both temperature and voltage are encountered at interfaces between stainless steel and graphite, even at the highest mechanical load level investigated.

Model reliability is further tested by comparing model results with experimental data obtained using samples III and IV and adopting operating conditions significantly different from those used during the fitting procedure. In particular, the I_{rms} value is decreased from 1200 to 670 and 980 A. It is worth noting that the sample geometry is also changed and, accordingly, a different Joule heat generation is expected to produce different temperature distribution, given that electric

resistance varies as a function of the cross-sectional surface area. For the same reason, voltage changes as well. Consistently, displacement resulting from thermal expansion varies with temperature departures from the initial value.

The obtained results are shown in Figures 20 and 21. One can observe that the developed model is able to entirely predict SPS system behavior in terms of temperature, voltage, and displacement temporal profiles. To further highlight the importance of taking into account contact resistances, Figure 21 shows model predictions when the fitted contact resistances are neglected (that is, model equations are solved by setting very high contact conductances). In this latter case, temporal profiles of temperatures and voltage are underestimated. As expected, the larger discrepancy is related to temperature taken in the axial position of the lower graphite small spacer, that is, the one closer to the relevant contact resistances. Moreover, cooling dynamics, occurring once the electric current is turned off, is overestimated so that displacement rises relatively too quickly to the initial value. It is apparent that sample IV has been chosen to make these considerations because, among samples investigated in this work, it is the most similar in size to the actual configuration used when sintering/synthesis experiments are performed.

Concluding Remarks

A quantitative description of the SPS system behavior in the case of the absence of powders has been addressed herein within the framework of a novel heuristic approach. In particular, electric and thermal resistances in horizontal contacts as functions of temperature and applied mechanical load have been obtained by direct comparison between model results and experimental data. The electric behavior of the system is described in detail by highlighting the importance of considering rms electric current and voltage (whichever pulse cycle is adopted) when the Joule effect needs to be quantitatively determined. For the first time model reliability is tested by comparing model predictions with experimental data obtained

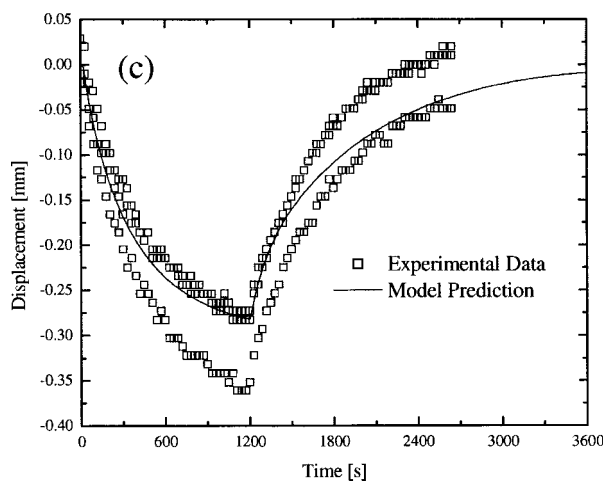
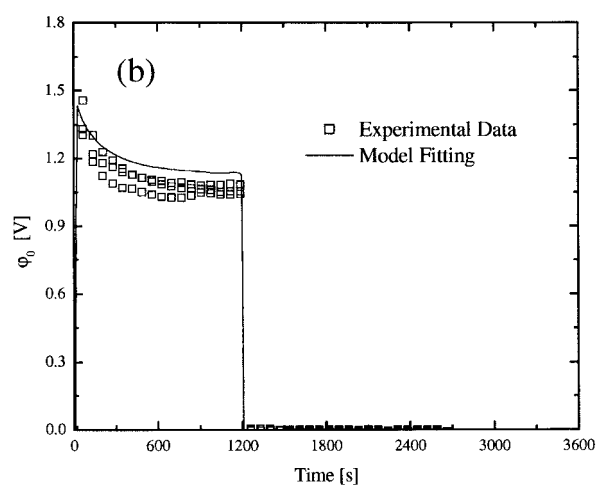
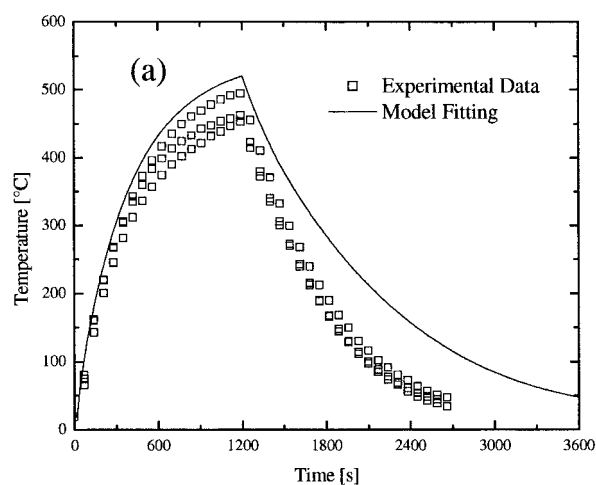


Figure 16. Comparison between experimental data and model results with respect to temporal profiles of temperature (a) taken at the center of the lower big spacer ($r = 0$, $z = 28$ cm), resistive portion of rms voltage (b), and displacement (c), when sample I is submitted to rms electric current step of 1200 A for 20 min, with a load of 3 kN.

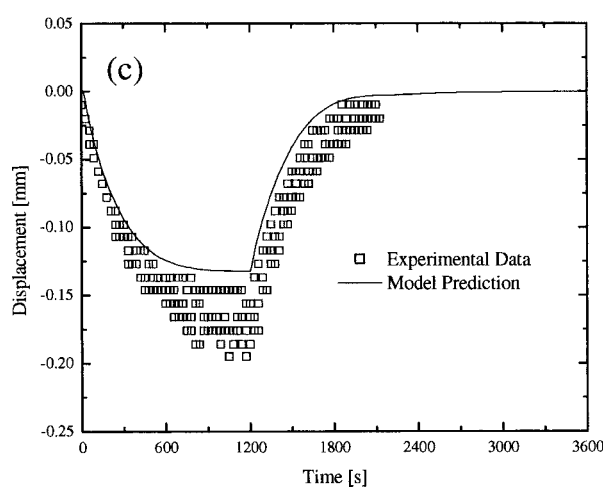
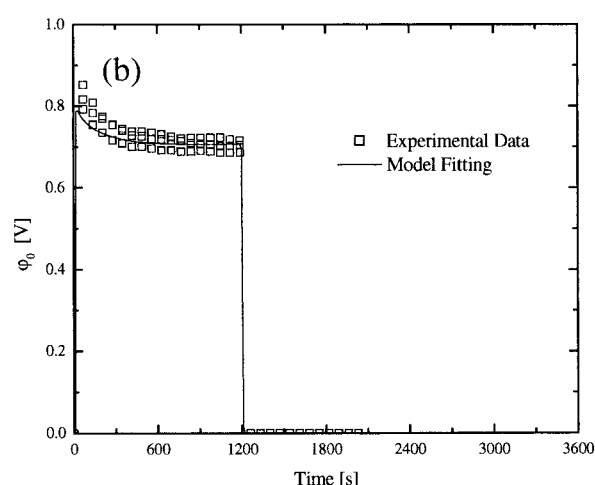
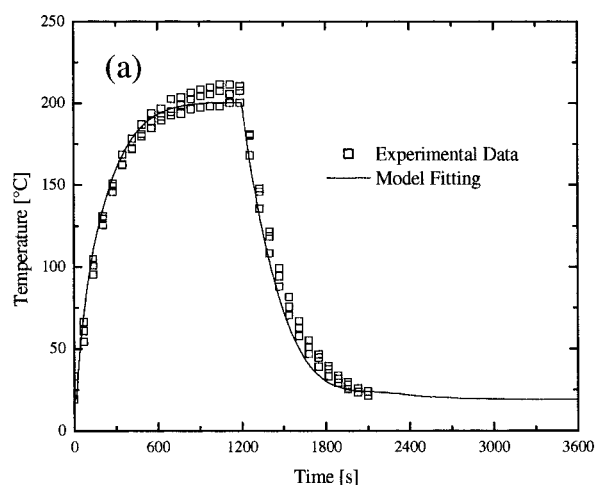


Figure 17. Comparison between experimental data and model results with respect to temporal profiles of temperature (a) taken at the center of the lower big spacer ($r = 0$, $z = 28$ cm), resistive portion of rms voltage (b), and displacement (c), when sample I is submitted to rms electric current step of 1200 A for 20 min, with a load of 30 kN.

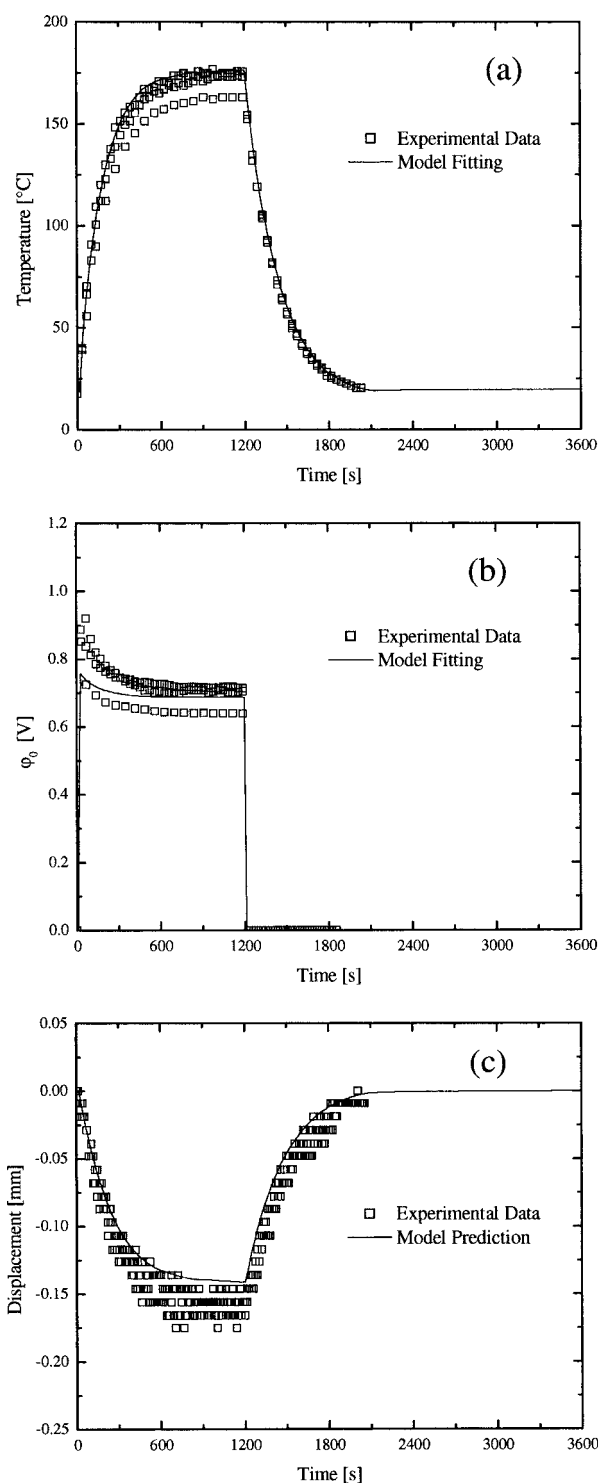


Figure 18. Comparison between experimental data and model results with respect to temporal profiles of temperature (a) taken at the center of the lower big spacer ($r = 0$, $z = 28$ cm), resistive portion of rms voltage (b), and displacement (c), when sample I is submitted to rms electric current step of 1200 A for 20 min, with a load of 50 kN.

Table 3. Fitted Parameters of Contact Conductances along with 95% Confidence Band and Correlation Coefficient R

Parameter	Value \pm SE	R
α_T	$22,810 \pm 4.6$ (m^{-1})	0.9368
β_T	1.08 ± 0.23	
α_E	64 ± 1.38 (m^{-1})	0.9609
β_E	0.35 ± 0.05	

at operating conditions significantly different from those considered during the fitting procedure. The proposed model has been successfully compared from a quantitative standpoint to the measured temperature, voltage, and displacement when rms current, geometry, and initial mechanical load are set. This work represents the first step toward the development of a complete model for the simulation of SPS system behavior where sintering/synthesis of powders sample takes place. The determination of graphite-graphite contact resistances in the vertical position between the plunger and the die, as well as the simulation of sintering/synthesis phenomena, will be examined in future investigations.

Notation

- a_n = Fourier series coefficient, A
- b_n = Fourier series coefficient, A
- C_E = electric contact conductance, $\Omega^{-1} \text{m}^{-2}$
- $C_{p,G}$ = graphite heat capacity, $\text{J kg}^{-1} \text{K}^{-1}$
- $C_{p,ss}$ = stainless steel heat capacity, $\text{J kg}^{-1} \text{K}^{-1}$
- C_T = thermal contact conductance, $\text{W m}^{-2} \text{K}^{-1}$
- E_G = graphite Young's modulus, N mm^{-2}
- E_{ss} = stainless steel Young's modulus, N mm^{-2}
- F = mechanical load, N
- f = fraction of localized Joule heat arising from electric contact resistance
- f_n = Fourier series frequency, s^{-1}
- H_G = graphite hardness, N m^{-2}

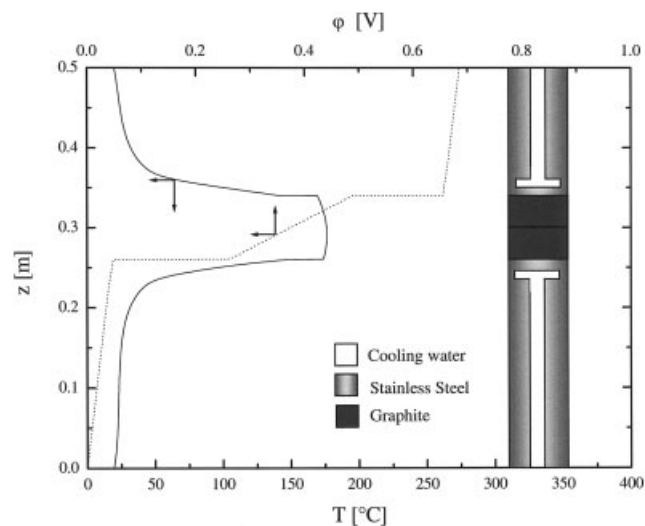


Figure 19. Axial profiles of temperature and resistive portion of rms voltage ($r = 3$ cm; $t = 20$ min) when sample I is submitted to rms electric current step of 1200 A for 20 min, with a load of 50 kN.

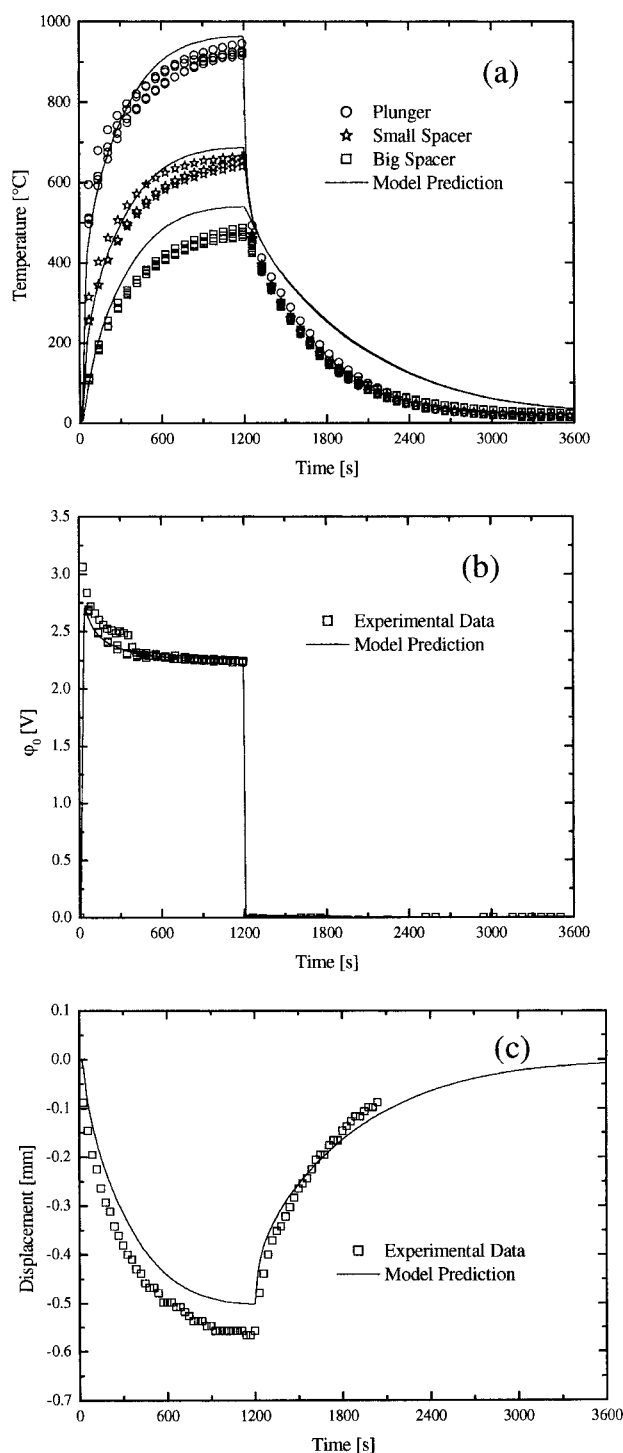


Figure 20. Comparison between experimental data and model predictions with respect to temporal profiles of temperature (a), resistive portion of rms voltage (b), and displacement (c), when sample III is submitted to rms electric current step of 670 A for 20 min, with a load of 3.5 kN.

Temperature is taken at three different locations: center of lower big spacer ($r = 0$, $z = 28$ cm), center of lower small spacer ($r = 0$, $z = 31.5$ cm), and center of plunger ($r = 0$, $z = 34$ cm).

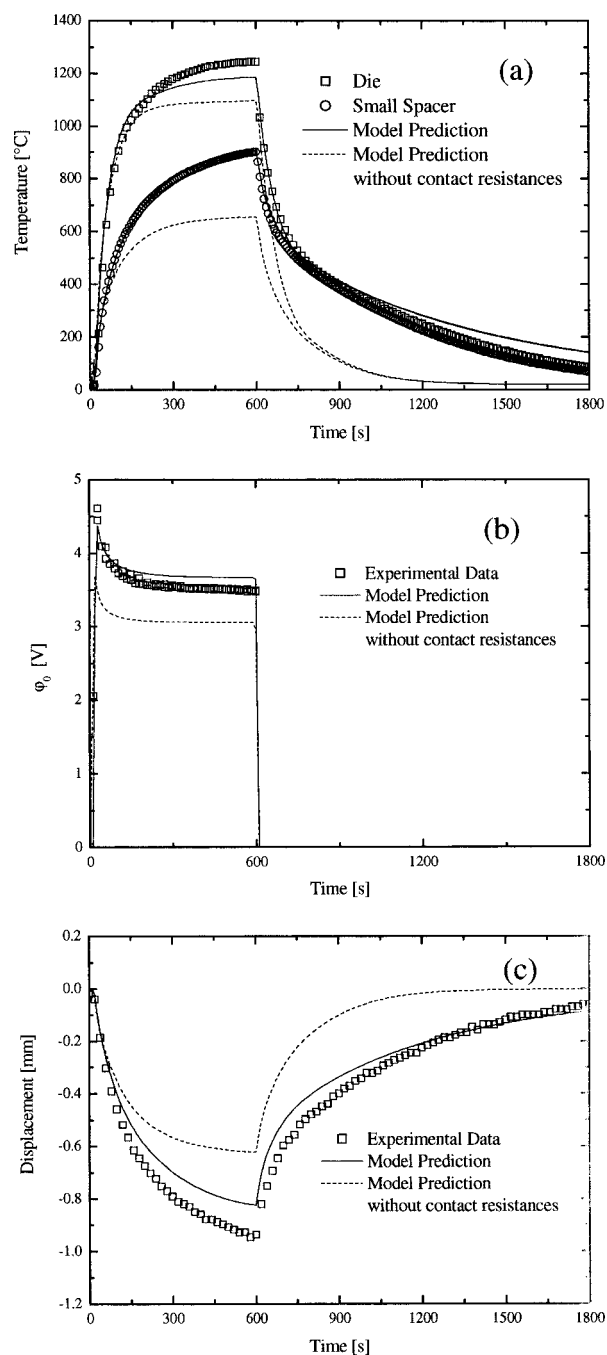


Figure 21. Comparison between experimental data and model predictions in terms of temporal profiles of temperature (a), resistive portion of rms voltage (b), and displacement (c), when sample IV is submitted to rms electric current step of 980 A for 10 min, with a load of 3.5 kN.

Temperature is taken at two different locations: center of lower small spacer ($r = 0$, $z = 31.5$ cm) and inside the die ($r = 1.1$, $z = 32.25$ cm).

H_{Harm} = harmonic mean between graphite and stainless steel hardness, $N\ m^{-2}$
 H_{ss} = stainless steel hardness, $N\ m^{-2}$
 h = heat transfer coefficient, $W\ m^{-2}\ K^{-1}$
 I = instantaneous electric current, A
 \bar{I} = temporal average electric current, A
 I_{rms} = temporal root mean squared electric current, A
 j = rms current density, $A\ m^{-2}$
 k_G = graphite thermal conductivity, $W\ m^{-1}\ K^{-1}$
 k_{Harm} = harmonic mean between graphite and stainless steel thermal conductivities, $W\ m^{-1}\ K^{-1}$
 k_{ss} = stainless steel thermal conductivity, $W\ m^{-1}\ K^{-1}$
 L = self-inductance, H
 \vec{n} = surface area unit vector in outward direction
 P = applied mechanical pressure, $N\ m^{-2}$
 \bar{P} = average power dissipated by electric circuit, W
 q_c = heat flux arising from thermal contact resistance, $W\ m^{-2}\ K^{-1}$
 q_e = localized Joule heat flux arising from electric contact resistance, $W\ m^{-2}\ K^{-1}$
 r = radial coordinate, m
 R = electric resistance, Ω
 S = surface area, m^2
 T = temperature, K
 T_0 = initial ambient temperature, K
 t = time, s
 u_r = radial displacement, m
 u_z = axial displacement, m
 V = instantaneous voltage, V
 \bar{V} = temporal average voltage, V
 V_L = instantaneous inductive voltage, V
 V_R = instantaneous resistive voltage, V
 V_{rms} = temporal root mean squared voltage, V
 ω_n = Fourier series angular velocity, $rad\ s^{-1}$
 X_L = inductive reactance, Ω
 z = axial coordinate, m

Greek letters

α_E = adjustable parameter in Eq. 9, m
 α_G = graphite coefficient of thermal expansion, K^{-1}
 α_{ss} = stainless steel coefficient of thermal expansion, K^{-1}
 α_T = adjustable parameter in Eq. 8, m
 β_E = adjustable parameter in Eq. 9
 β_T = adjustable parameter in Eq. 8
 ϵ_r = strain tensor normal component in radial direction
 ϵ_z = strain tensor normal component in axial direction
 ϕ = resistive rms voltage, V
 ϕ_0 = resistive rms voltage between electrodes ends, V
 γ_{zr} = strain tensor tangential component
 η_G = graphite emissivity
 η_{ss} = stainless steel emissivity
 v = Stefan-Boltzmann constant, $W\ m^{-2}\ K^{-4}$
 ρ_G = graphite density, $kg\ m^{-3}$
 ρ_{ss} = stainless steel density, $kg\ m^{-3}$
 $\rho_{el,G}$ = graphite electric resistivity, $\Omega\ m$
 ρ_{Harm} = harmonic mean of graphite and stainless steel electric resistivities, $\Omega\ m$
 $\rho_{el,ss}$ = stainless steel electric resistivity, $\Omega\ m$
 $\sigma_{el,G}$ = graphite electric conductivity ($= 1/\rho_{el,G}$), $\Omega^{-1}\ m^{-1}$
 $\sigma_{el,Harm}$ = harmonic mean of graphite and stainless steel electric conductivities, $\Omega^{-1}\ m^{-1}$
 $\sigma_{el,ss}$ = stainless steel electric conductivity ($= 1/\rho_{el,ss}$), $\Omega^{-1}\ m^{-1}$
 σ_r = stress tensor normal component in radial direction, $N\ mm^{-2}$
 σ_z = stress tensor normal component in axial direction, $N\ mm^{-2}$
 τ = sampling time, s
 τ_{zr} = stress tensor tangential component, $N\ mm^{-2}$
 ν_G = graphite Poisson's ratio
 ν_{ss} = stainless steel Poisson's ratio

Acknowledgments

The financial support of Namamet (VI Program Framework) and CyberSar projects is gratefully acknowledged. The authors also thank

Prof. Silvano Cincotti of Dipartimento di Ingegneria Biofisica ed Elettronica, Università degli Studi di Genova, Italy, for his fruitful help.

Literature Cited

- Omori M. Sintering, consolidation, reaction and crystal growth by the spark plasma sintering system (SPS). *Mater Sci Eng.* 2000; A287:183–188.
- Groza JR, Zavaliangos A. Sintering activation by external electrical field. *Mater Sci Eng.* 2000;A287:171–177.
- Locci AM, Orrù R, Cao G. Simultaneous spark plasma synthesis and consolidation of WC/Co composites. *J Mater Res.* 2005;20:734–741.
- Yucheng W, Zhengyi F. Study of temperature field in spark plasma sintering. *Mater Sci Eng.* 2002;B90:34–37.
- Xie G, Ohashi O, Chiba K, Yamaguchi N, Song M, Furuya K, Noda T. Frequency effect on pulse electric current sintering process of pure aluminum powder. *Mater Sci Eng.* 2003;A359:384–390.
- Dobedoe RS, West GD, Lewis MH. Spark plasma sintering of ceramics: Understanding temperature distribution enables more realistic comparison with conventional processing. *Adv Appl Ceram.* 2005; 104:110–116.
- Chen W, Anselmi-Tamburini U, Garay JE, Groza JR, Munir ZA. Fundamental investigation on the spark plasma sintering/synthesis process. I. Effect of dc pulsing on reactivity. *Mater Sci Eng.* 2005;A394:132–138.
- Vanmeensel K, Laptev A, Hennicke J, Vleugels J, Van der Biest O. Modelling of the temperature distribution during field assisted sintering. *Acta Mater.* 2005;53:4379–4388.
- Anselmi-Tamburini U, Gennari S, Garay JE, Munir ZA. Fundamental investigation on the spark plasma sintering/synthesis process. II. Modeling of current and temperature distributions. *Mater Sci Eng.* 2005;A394:139–148.
- Weissler GA. Resistance sintering with alumina dies. *Int J Powder Metall.* 1981;17:107–118.
- Zavaliangos A, Zhang J, Krammer M, Groza JR. Temperature evolution field activated sintering. *Mater Sci Eng.* 2004;A379:218–228.
- Heian EM, Feng A, Munir ZA. A kinetic model for the field-activated synthesis of MoSi₂/SiC composites: Simulation of SPS conditions. *Acta Mater.* 2002;50:3331–3346.
- Fano RM, Chu LJ, Adler RB. Electromagnetic Fields, Energy, and Forces. New York: John Wiley & Sons; 1959.
- Perry RH, Green D. Perry's Chemical Engineers' Handbook. 6th Edition. New York: McGraw-Hill; 1984.
- Barin I. Thermochemical Data of Pure Substances. New York: VCH; 1993.
- Touloukian YS. Thermophysical Properties of High Temperature Solid Materials. New York: Macmillan; 1967.
- ASM International. High-Temperature Property Data: Ferrous Alloys. Materials Park, OH: ASM International; 1988.
- CRC. Materials Science and Engineering Handbook. 3rd Edition. Boca Raton, FL: CRC Press; 2001.
- IIT Research Institute. Handbook of Thermophysical Properties of Solid Materials. New York: Macmillan; 1961.
- Peters RL. Materials Data Nomographs. New York: Reinhold Publishing/Chapman & Hall; 1965.
- Goldsmith A, Waterman TE, Hirschhorn HJ. Handbook of Thermophysical Properties of Solid Materials. Oxford, UK: Pergamon Press; 1961.
- Incropera FP, DeWitt DP. Fundamentals of Heat and Mass Transfer. New York: John Wiley & Sons; 1981.
- CRC. Handbook of Chemistry and Physics. 80th Edition. Boca Raton, FL: CRC Press; 2000.
- Duffin WJ. Electricity and Magnetism. 3rd Edition. London: McGraw-Hill; 1980.
- Madhusadana CV. Thermal Contact Conductance. New York: Springer-Verlag; 1996.
- Babu SS, Santella ML, Feng Z, Riemer BW, Cohron JW. Empirical model of effects of pressure and temperature on electrical contact resistance of metals. *Sci Technol Weld Joining.* 2001;6:126–132.

Manuscript received Feb. 22, 2006, revision received Aug. 31, 2006, and final revision received Dec. 12, 2006.